Particle-in-Cell Simulations of Sheath Formation Around Biased Interconnectors in a Low-Earth-Orbit Plasma

H. Thiemann*
Physikalisch-Technische Studien GmbH
Freiburg, Federal Republic of Germany
and
R. W. Schunk†
Center for Atmospheric and Space Sciences
Utah State University, Logan, Utah 84322

Particle-in-cell simulations were performed to study the interaction between a solar array and the low-earth-orbit (LEO) plasma. In the calculations, a potential was suddenly applied to the solar cell interconnector, and the subsequent temporal response was followed for the real O^+-electron mass ratio. Simulations were conducted for both 100- and 250-V solar cells, an extended simulation system, different solar cell thicknesses, and solar cells with secondary electron emission. Initially, the solar cell cover glass acquires a positive polarization surface charge. Without secondary electron emission, this positive surface charge is neutralized by plasma electrons that are attracted to the cover glass, and eventually an equilibrium is reached with a slightly negative potential on the cover glass. During the same time period, the plasma electrons also act to shield the interconnector, and in the steady state, a distinct localized sheath surrounds the interconnector. Larger applied potentials and thinner solar cells lead to greater initial polarization surface charges and, hence, longer discharging and shielding times, but otherwise the physics is unchanged. However, with secondary electron emission from the cover glass, the physics is completely different. The potential structure over the interconnector and solar cells is almost planar, which allows for a continual interaction between the plasma electrons and the cover glass. A large fraction of the resulting secondary electrons is collected by the interconnector, which amounts to an order of magnitude increase in the collected current. Model calculations are a useful tool for studying the interaction processes between the LEO plasma and biased solar arrays. The simulations suggest new aspects for further laboratory tests, define an efficient mode of operation for solar arrays, and can provide design guidelines for solar arrays with respect to material properties.

Nomenclature

d = cover glass thickness
E = primary electron impact energy
E^+ = electric field outside dielectric
E^- = electric field inside dielectric
M_e = electron mass
M_i = ion mass
N_e = electron density
$R_\parallel$ = sheath radius parallel to solar cell
$R_\perp$ = sheath radius perpendicular to solar cell
R_{sh} = sheath radius of a simple probe
t = time
T = normalized time (in units of ω_{pe}^{-1})
T_e = electron temperature
x,y = spatial coordinates
Y_e = secondary electron yield
ϵ = dielectric permittivity
θ = incident angle measured from normal
λ_d = electron Debye length
σ_{ext} = free charge on dielectric surface
ϕ = electrostatic potential
ϕ_0 = applied interconnector potential
ω_{pe} = electron plasma frequency

Received Sept. 16, 1988; revision received Oct. 11, 1989.

*Senior Research Scientist.
†Director of CASS.

I. Introduction

THE efficient design of high-voltage solar array (HVSA) operating in the low-earth-orbit (LEO) environment is of particular importance with respect to electrical efficiency and weight. Voltages of several hundred volts are envisaged in order to minimize resistive losses in the solar array bus lines. High voltages, however, may lead to undesirable interactions between exposed surfaces and the ambient plasma, causing degradation effects on solar cell material due to arc discharges or power drain due to leakage currents flowing through the plasma.[1]

Leakage current phenomena were studied in a series of experimental[1-8] and theoretical[9-12] investigations. At a certain positive voltage, solar arrays were found to draw increased current. Such an anomalously enhanced current collection of solar array interconnectors at a not clearly understood voltage onset emphasizes the deviation from simple Langmuir probe behavior. Since normal current collection of such probes only involves particles from the ambient plasma, a new source of particles is required to explain the increased currents. It is the general understanding that secondary electron emission from solar cell surfaces provides these additional charge carriers. The specific solar array structure, combining conducting and dielectric parts, is considered to favor the formation of electric fields that energize plasma electrons toward dielectric surfaces. Depending on the energy and the angle of incidence, these accelerated electrons can cause secondary electron emission, and the generated electrons are eventually collected by the interconnectors. The electric fields are due to a special sheath formation around the biased interconnectors. The dimensions of the measured sheath were typically one order of magnitude smaller[5,8] than those expected from Langmuir-Child considerations for a spherical geometry.[2] For high den-

sities, the sheath becomes so small that there is no direct experimental evidence of the internal potential distribution.[8] This experimental result contradicts a recent model based on the assumption that the sheath thickness is generally larger than the interval between the interconnectors (solar cell width)[13] where the solar array is entirely covered by the sheath. This model, which identifies the array with a single conductive plate, suppresses small-scale processes. As will be shown, microscopic effects are important to explain increased current collection in the positive voltage range.

Particle-in-cell (PIC) simulations are extremely powerful for studying small-scale interaction processes in a plasma. Such calculations have already been performed for the so-called "pinhole" problem.[9-12] In these PIC simulations, a conducting disk was covered with a kapton insulator, except for a small circular region at the center of the disk (the pinhole), and the subsequent interaction of the positively biased conducting disk with the surrounding plasma was calculated. Simulations were performed both with and without secondary electron emission from the dielectric material. However, in order to save computer time, artificial ion masses, as low as the electron mass (i.e., $M_i/M_e = 1$), were used in the calculations. Nevertheless, the calculations confirmed the general trend of smaller sheath dimensions than predicted by simple probe theory. These calculations also supported the suggestion that the increased current collection was due to secondary electron emission from the dielectric surface.

The primary purpose of this paper is to demonstrate the feasibility of conducting realistic PIC simulations for the solar array/plasma interaction problem. The earlier simulations discussed above were limited in that only the pinhole problem was considered and artificial ion masses were used. In our simulations, on the other hand, we modeled a segment of a solar array, and we used the correct value of $M_i/M_e = 29{,}330$ for 0^+ at LEO altitudes. The use of a correct mass ratio is critical if one is interested in obtaining the temporal evolution of the plasma dynamics. Our model therefore gives a detailed picture of the physical processes (sheath formation, surface charges and potentials, collected current, etc.) as a function of time for the biased solar array problem. Such a detailed picture has not been presented previously.

The specific calculations presented here were stimulated by ground tests involving positively biased solar array test modules in a simulated LEO-plasma ($N_e = 10^5 - 10^6$ cm^{-3}, $T_e = 0.1$ eV).[8] The experimental results suggest that increased current collection is caused by characteristic shielding and charging processes around the biased interconnectors. Specifically, large electric fields are created near the edge of the solar cell cover glass, and impacting plasma electrons cause secondary electrons, which can be collected by the adjacent interconnector. The small-scale potential structure of the sheath cannot be resolved by standard probe techniques. Therefore, the empirical current collection model deduced by Ref. 8 has to be theoretically explained. In the following, we present results from two-dimensional PIC calculations that simulate a positively biased solar array embedded in a typical ionospheric plasma.

II. Model Description

The model takes advantage of the large number of identical solar cells in series connection. In such a configuration, there are small voltage gradients (≈ 0.5 V) on each side of the cell, but these are negligible for the applied voltages considered in this study (100 and 250 V). With the repetition of the same geometry, the numerical scheme shown in Fig. 1 concentrates on one solar cell unit with the conductive interconnector at the center of the bottom boundary. The processes occurring in the system are periodically repeated in the left and right directions. The grid system, for the identification of potential, electric field, and electron and ion densities at the grid points, uses a variable spacing with a higher resolution at locations close to the interconnector and the solar cell surface.

The following boundary conditions are applied to the potential and particles:

a) The lower boundary ($y = 0$) represents the solar cell surface with the exposed conductive interconnector in the center. The interconnector is biased to a prescribed positive potential ϕ_0. The cover glasses, as shown in Fig. 1, are attached to the also biased grid fingers. In a vacuum, such a configuration creates surface potentials on the cover glasses of the order of the applied potential. A minor potential reduction associated with induced positive surface charges occurs because of polarization effects in the cover glass material. The corresponding boundary condition is given by the electric field discontinuity at the cover-glass grid points,

$$E^+ - \epsilon E^- = \sigma_{\text{ext}} \tag{1}$$

where $\epsilon (= 4)$ is the dielectric constant of the cover glass.

b) The upper boundary ($y = y_{\max}$) describes the undisturbed plasma environment. We arbitrarily set the constant potential to zero, and this then represents the plasma potential,

$$\phi(x, y_{\max}) = 0 \tag{2}$$

c) The boundaries $x = 0$ and $x = x_{\max}$ characterize the periodic boundaries simulating the already mentioned infinite repetition of the given particle and potential structures in the x-direction. These boundaries describe identical conditions with

$$\phi(0, y) = \phi(x_{\max}, y) \tag{3}$$

Plasma particles are treated in the following way. At the beginning of the simulation ($t = 0$), the particles are uniformly distributed in the system to provide quasineutrality at the grid points of the system. Electrons and oxygen ions (the simulation used real ion masses!) are equipped with random velocities corresponding to typical ionospheric temperatures with Maxwellian features. Using a time-centered leapfrog scheme, the particles are advanced in time according to their inertia and the self-consistent electric fields. Particle tracking can result in the following interference with the boundaries. Particles hitting the interconnector region contribute to the collected current. Particles impacting on the dielectric cover-glass

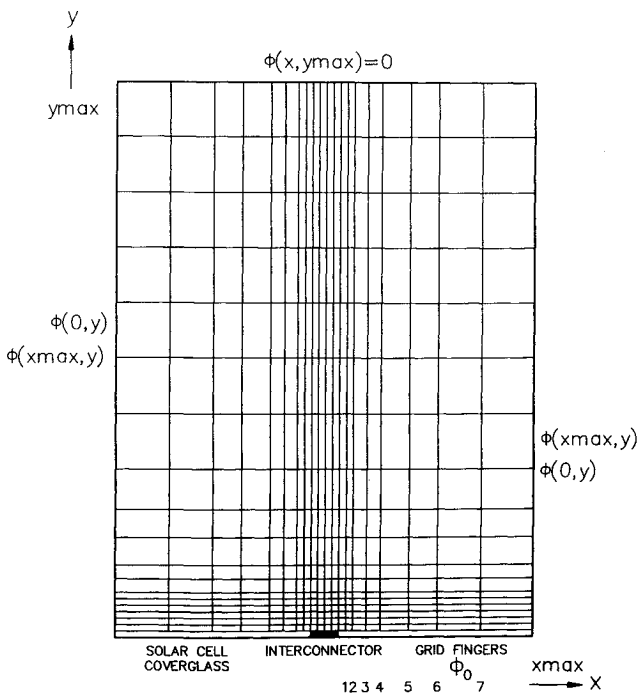

Fig. 1 Simulation grid for the solar cell model.

surface contribute to the surface charge. In the assumed undisturbed plasma environment, near the upper boundary, particles are allowed to leave the system. New particles are supplied from the upper boundary to simulate a random thermal current from the ionospheric plasma. Particles leaving through the periodic boundaries are conserved. A particle crossing $x = x_{max}$ out of the system with the coordinates (x,y) is reintroduced to the system at $(x - x_{max}, y)$. The corresponding velocity components do not change. An analogous scheme is applied for particles crossing the $x = 0$ boundary.

The code involves an option for secondary electron emission from the dielectric cover glasses, which normally carry an antireflexion coating of MgF_2 on the top. The dependence of the secondary electron yield on the primary impact energy E has been determined experimentally for MgF_2.[14] For energies $E < 400$ eV, the yield curve obtained from the measurement can be fit with the simple formula

$$Y_e^{MgF_2} = (0.036.E)^{1/2} \tag{4}$$

where E is in electron volts. This formula is valid for normal incidence primaries. However, in our experiments,[8] we empirically deduced a possible angle dependency for the emission of secondary electrons from the cover glasses, and, hence, we scaled Eq. (4) with a primary electron angle dependency that was parametrically chosen as $\cos^{-1}\theta$, $\cos^{-1/2}\theta$, and 1. This scaling is also suggested in standard textbooks. In our simulations, the emitted secondary electrons are supplied with random thermal energies, which also determine a random emission angle with respect to the target.

III. Solar Cell Simulations

The model calculations performed to study the interaction between a solar array and the LEO plasma are listed in Table 1. For typical ionospheric plasma conditions ($N_e = 5.5 \times 10^6$ cm^{-3} and $T_e = 0.1$ eV), simulations were conducted for positive solar cell voltages of 100 and 250 V. The latter case was repeated for an extended system in the y-direction and for a thinner solar cell cover glass. Also, for the 250-V case, secondary electron emission from the solar cell cover glass was considered, and three primary electron angle dependencies were modeled.

A. Sheath Formation

We first present the simulations that did not include secondary emission. In Fig. 2 we show the temporal evolution of the potential in the simulation system for an applied interconnector potential $\phi_0 = 100$ V that is instantly switched on. The potential contours are plotted with a time increment of $T = 50$ (0.38 μs). The location of the interconnector is at the center of the bottom boundary. At $T = 0$, the quasineutrality of the ambient plasma determines the vacuum potential distribution, which exhibits essentially planar equipotential lines. Only close to the interconnector is there a small deviation from this planar behavior. As already mentioned, polarization effects in the dielectric cover glass cause positive induced surface charges on the dielectric, which act to slightly reduce the surface potential. To reach quasi-steady-state conditions, the vacuum electric field has to be widely neutralized in the system. The surface potential on the cover glass cannot be shielded as in the case of the metallic interconnector. Therefore, in the dynamic evolution, the plasma acts to reduce the dielectric surface potential. The mechanism responsible for field neutralization is suggested by Fig. 2. The initial electric field accelerates ions toward the upper boundary, and electrons are attracted to the solar cell surface material. Electrons discharge the positive surface charge of the dielectric decreasing simultaneously the positive surface potential. The interaction between the dielectric and plasma eventually approaches an equilibrium with a slightly negative surface potential on the dielectric. Simultaneously, the biased interconnector is shielded by the plasma. The sheath formation is generated by a contraction of the potential structure. Asymptotically, the sheath approaches a quasi-steady state with defined sheath dimensions. Outside the sheath, the electric field is completely neutralized. This fact suggests that for the cases without emission, the choice of the upper boundary is not important for the final solution of our interaction problem.

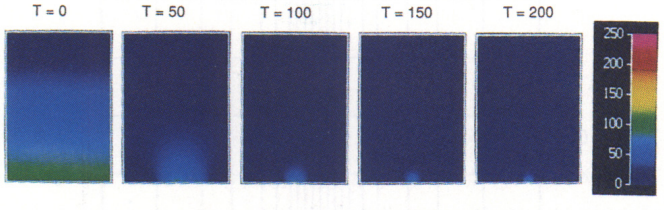

Fig. 2 Potential distribution at selected times after a series of 100-V solar cells is switched on; the times are in units of ω_{pe}^{-1}.

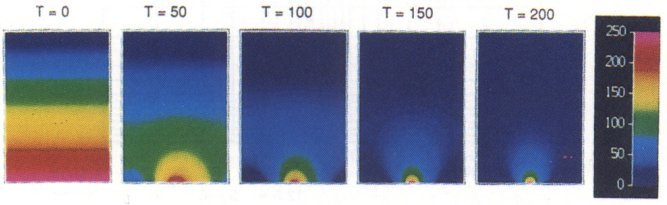

Fig. 3 Potential distribution at selected times after a series of 250-V solar cells is switched on; the times are in units of ω_{pe}^{-1}.

Similar processes are observed for an increased potential of $\phi_0 = 250$ V applied to the interconnector. Figure 3 shows the corresponding sequence of potential contours. The formation phase of the sheath and the dielectric discharging phenomena are qualitatively similar to that shown in Fig. 2. The temporal evolution, however, shows that increased applied potentials result in longer times for the discharging and shielding processes due to the enhanced induced surface charges.

The effect of a longer system is demonstrated in Fig. 4. With a doubled y-dimension and $\phi_0 = 250$ V, there are no new aspects to the interaction, except that we observe a longer formation phase of the potential structure. The vacuum electric fields are smaller for the larger system. Therefore, it takes longer for the electrons to reach the cell surfaces to discharge the polarization charges and to reduce the associated surface potentials. The steady state, however, displays the same

Table 1 List of simulation runs, for all cases $\lambda_d = 0.1$ cm, $T_e = 0.1$ eV, and $N_e = 5.5 \times 10^6$ cm^{-3}

Run	System size ($\lambda^2{}_d$)	ϕ_0 (V)	SEE	d (cm)
PMI100	1.5×2	100	0	0.1
PMI250	1.5×2	250	0	0.1
PMIEX250	1.5×4	250	0	0.1
PMIDYO	1.5×2	250	0	0.015
PMIEM	1.5×2	250	$\cos^{-1}\theta$	0.1
PMIEC	1.5×2	250	$\cos^{-1/2}\theta$	0.1
PMIEC1	1.5×2	250	1	0.1

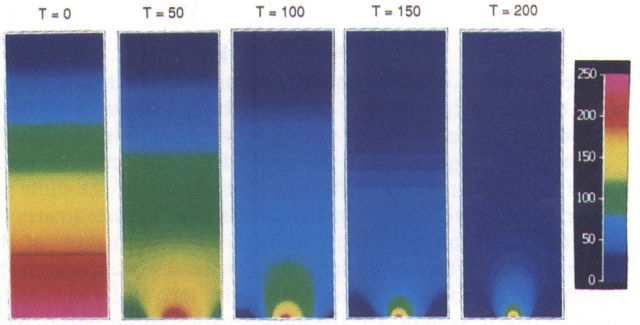

Fig. 4 Potential distribution at selected times after a series of 250-V solar cells is switched on; this case is the same as for Fig. 3 except that the simulation domain is extended in the y-direction time in units of ω_{pe}^{-1}.

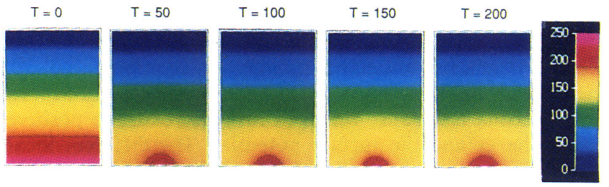

Fig. 5 Potential distribution at selected times after a series of 250-V solar cells is switched on; secondary electron emission ($\cos^{-1}\theta$) from the solar cell cover glass is included in this simulation, time in units of ω_{pe}^{-1}.

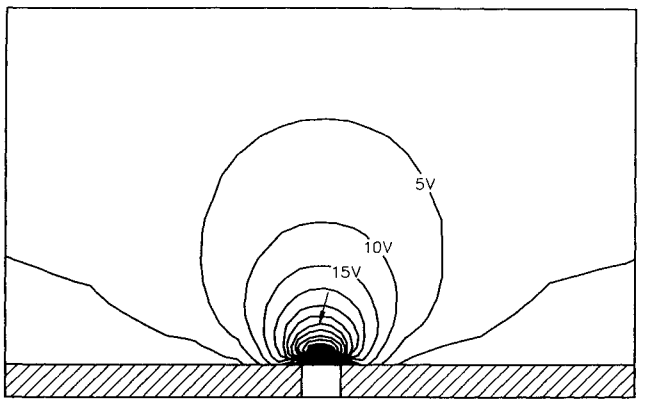

Fig. 6a Sheath structure for a solar cell potential of 100 V; the arrow indicates the location where the potential decreases to $\phi_0/2.718$.

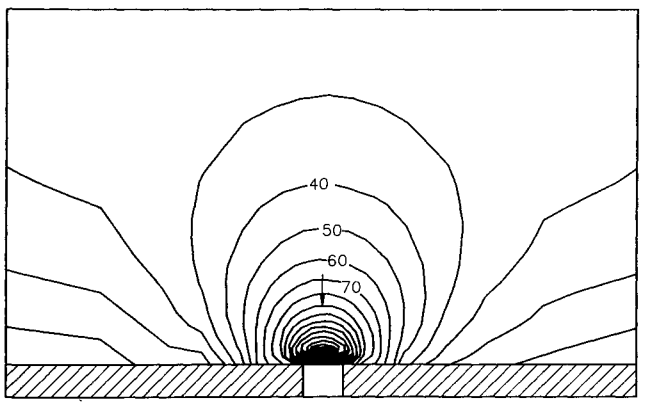

Fig. 6b Sheath structure for a solar cell potential of 250 V; the arrow indicates the location where the potential decreases to $\phi_0/2.718$.

potential structure as the smaller system. For the adopted set of plasma parameters, the space outside the interconnector sheath is field-free, and therefore the calculations with a larger system emphasize that the interaction results are not very sensitive to the chosen system dimensions.

As will be shown later, the discharging of the initially biased dielectric surfaces is an important mechanism in the interaction between solar cells and the plasma. The discharging time depends on the initial electric fields, which are a function of the system size in the y-direction and the applied potential ϕ_0, and the induced positive surface charges, which are defined by ϵ and the cover glass thickness d. The discharging is especially long for a realistic cover glass thickness of $d = 0.015$ cm; the potential structure at $T = 200$ (1.5 μs) differs only slightly from the vacuum structure (run labeled PMIDYO in Table 1).

The next simulations included secondary electron emission from the dielectric surfaces, which has a dramatic effect on dielectric discharging. Figure 5 shows the evolution of the potential structure for the case with a $\cos^{-1}\theta$ angle dependence for the secondary electron yield. Note that in this case a quasi-steady state is achieved as early as $T = 50$ (0.38 μs). In contrast to nonemitting surfaces, the related potentials are now

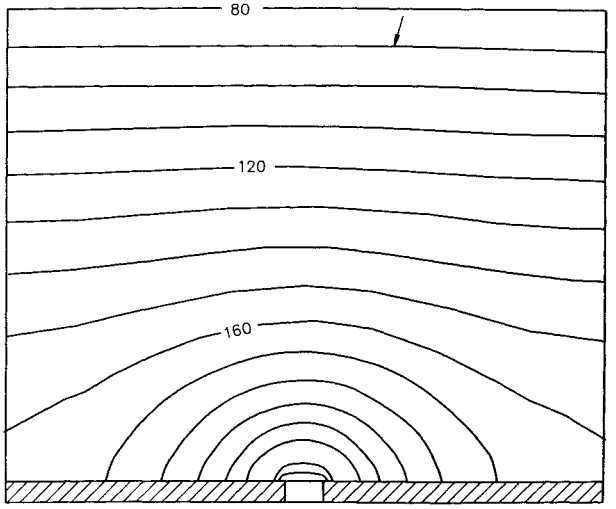

Fig. 6c Sheath structure for a solar cell potential of 250 V and secondary electron emission ($\cos^{-1}\theta$); the arrow indicates the location where the potential decreases to $\phi_0/2.718$.

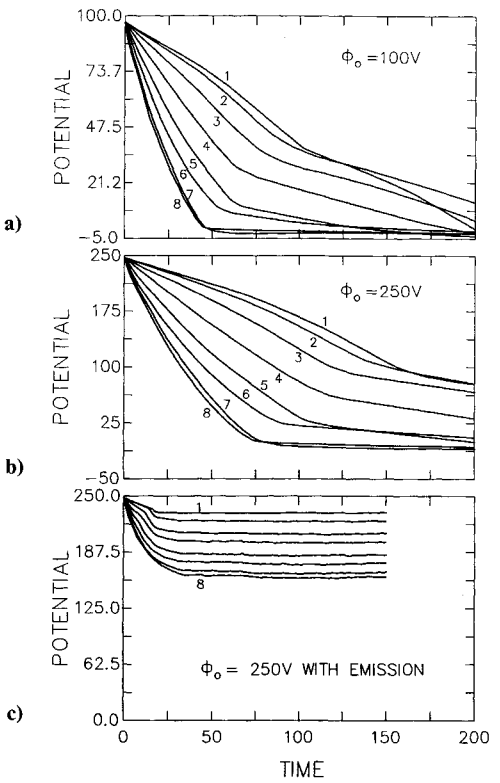

Fig. 7 Temporal evolution of the surface potential at several locations along the solar cell: a) for $\phi_0 = 100$ V, b) $\phi_0 = 250$ V, and c) $\phi_0 = 250$ V with secondary electron emission.

rather large: $\phi = 150$ V. With the emission of electrons, all over the cover glass surface, the current balance is maintained with the plasma particles even at high surface potentials.

The sheath dimensions for the various cases are shown in Figs. 6a–6c and are summarized in Table 2. The sheath radius is defined at the location where the potential drops to the value $\phi_0/2.718$ and is shown by the arrow. The sheath radius in the y-direction ($R_\perp$) agrees with normal probe theory in that it increases with the applied potential and decreases with the plasma density. However, the extent of the sheath is of the order of the Debye length, and this does not agree with standard sheath predictions for a spherical probe (R_{sh}). With the inclusion of secondary electron emission, the physical situation changes completely, and normal probe theory is no longer ap-

plicable. Note that without emission, the shielding of the interconnector is very efficient with almost no overlapping of the sheath potential contours on the cover glass (small values of $R_{\parallel}$). With emission, on the other hand, the potential structure is almost planar ($R_{\parallel} \to \infty$), and this allows for a continual interaction between the ambient plasma and the secondary electrons. Although these potentials look similar to those in the "snapover" model with overlapping of sheath structures,[4] the processes leading to our planar potentials are completely different. Finally, we note that the other emission cases in Table 1 ($\cos^{-1/2}\theta$ and 1) display similar characteristic values for ϕ, $R_{\parallel}$ and $R_{\perp}$ to those presented above for a $\cos^{-1}\theta$ angle dependence for secondary electron emission.

B. Surface Charges and Potentials

Current collection is controlled by the processes occurring on the dielectric surface. Figures 7a–7c show the temporal evolution of the dielectric surface potential and Figs. 8a–8c show the corresponding surface charges. Successively, we see from the top the cases for an interconnector potential of +100 V (Figs. 7a and 8a), +250 V (Figs. 7b and 8b) and +250 V including secondary emission (Figs. 7c and 8c). The eight curves refer to different locations on the cover glass, where the numbers are explained in Fig. 1. Therefore, curve 1 is for the location closest to the interconnector, and curve 8 describes the behavior in the center of the solar cell. The comparison of Figs. 7 and 8 emphasizes the direct relationship between the dielectric surface potential and the surface charge.

For the nonemitting case with $\phi_0 = 100$ V (Figs. 7a and 8a), the following scenario becomes evident: At $t = 0$, the surface has a constant positive polarization charge density. Its magnitude depends on the applied potential. The associated surface potential is close to the applied interconnector potential. As time elapses, the interaction with the ambient plasma acts to attract plasma electrons, which in turn decrease the positive surface charge and the surface potential. The different locations on the cover glass display different discharging features. Qualitatively, we can identify three distinct regions. Region 1, including locations 7 and 8 in the solar cell center, is unaffected by the sheath and shows a straight discharging behavior. The center becomes completely discharged and finally attains a negative space charge and potential. At this stage, the discharging process is abruptly stopped with a constant potential of −2 V and constant surface charge density. This part of the solar cell reaches an equilibrium with the ambient plasma as though it were an isolated dielectric. Curves 2 to 6 describe in the intermediate region (Region 2) where the discharging depends on the sheath formation. The knee in the curves is due to a reduction of discharging particles. It appears at successively later times in the evolution as we approach the interconnector. Here, we note the direct influence of the contacting sheath. Eventually, as shown by curves 5 and 6, the intermediate region also reaches an equilibrium with the thermal plasma at a potential of −2 V. Close to the interconnector (in the contact Region 3), a very efficient discharging of the cover glass takes place at $T = 100$. Then, plasma electrons are very efficiently focused towards the interconnector with an enhanced discharge rate near the edges of the cover glasses.

Figs. 7b and 8b show a comparable behavior for $\phi_0 = +250$ V. The initially larger positive polarization charges, of course, are discharged at a slower rate by the same surrounding plasma environment. The three discharging regions can be clearly identified. The strong discharging in the contact region starts at around $T = 175$ (1.3 μs).

A smaller solar cell thickness (see Table 1, run PMIDYO) is characterized by larger positive surface polarization charges. With the same number of negative charge carriers offered by the given plasma environment, the duration of the discharging

Table 2 Sheath radii R (cm) derived from computer simulations (R_{sh}: simple probe sheath radius)

ϕ_0	$\phi_0/2.718$	SEE	$R_{\perp}$/sim	$R_{\parallel}$	R_{sh}
100	37	—	0.11	0	4.5
250	92	—	0.17	0.03	6.7
250	92	$\cos^{-1}\theta$	1.09	∞	6.7

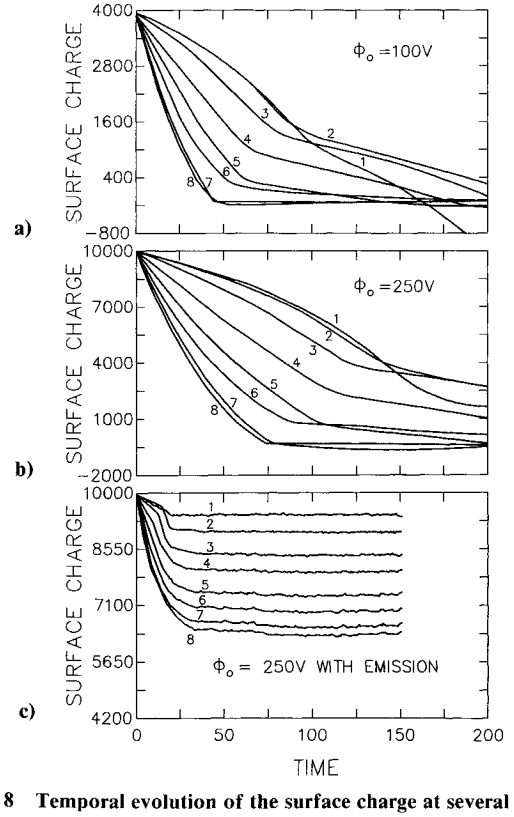

Fig. 8 Temporal evolution of the surface charge at several locations along the solar cell: a) for $\phi_0 = 100$ V, b) $\phi_0 = 250$ V, and c) $\phi_0 = 250$ V with secondary electron emission.

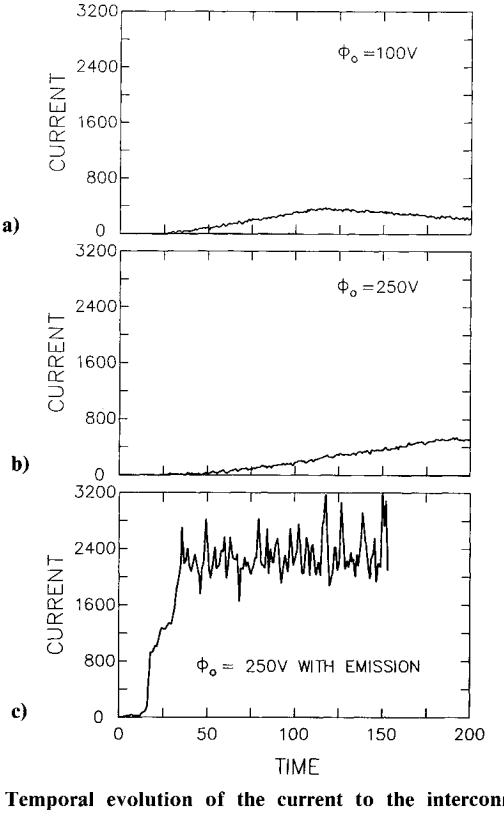

Fig. 9 Temporal evolution of the current to the interconnector: a) for $\phi_0 = 100$ V, b) $\phi_0 = 250$ V, and c) $\phi_0 = 250$ V with secondary electron emission.

of the dielectric surface increases correspondingly without new physical features.

For the emitting solar cell surface, the situation changes completely (Figs. 7c and 8c). The initial phase almost identically follows the nonemitting case, and we note a collective behavior starting at $T = 30$ (0.225 μs) with a constant surface potential and charge density. The transition from nonemitting conditions at $T = 20$ (0.15 μs) to emitting conditions at $T = 30$ is characterized by a more rapid decrease of the potential and surface charge density.

C. Current Collection

The information pertaining to the number of particles collected by the interconnector is given in Figs. 9a–9c. Successively, we see the same cases as in Figs. 7 and 8. We noted in Section III.A that without secondary electron emission the potential contours change from planar to circular-shaped structures around the interconnector as time proceeds. This results in the electron current variation shown in Fig. 9a. The current first increases, reaches a maximum at around $T = 100$ (0.75 μs), then decreases, and finally approaches a steady-state value. Plasma electrons first move in a laminar fashion to the surface to discharge the dielectric, but later they interact with the sheath potential and are diverted towards the interconnector. All electrons entering the sheath region therefore contribute to the collected current. With increased shielding and a corresponding decrease in the sheath radius, the number of electrons that enter the sheath decreases, along with the collected current. A constant current value, controlled by the thermal electron current outside the sheath, is obtained after the sheath has finally formed.

Qualitatively similar results are observed for $\phi_0 = 250$ V. A current maximum becomes visible at the end of the simulation with a slightly decreasing current afterwards. As discussed in III.B, this longer rise time of the current is related to the discharging of the initially larger surface polarization charge density. The current maximum is reached at the time when discharging the contact region increases sharply (Fig. 8a, curve 1).

Different features are seen when secondary electron emission is included. Initially, the evolution of the current is similar to the nonemitting case. A sudden steep increase in the current occurs at $T = 20$ (0.15 μs), and this is followed by a transition region that lasts until $T = 35$ (0.26 μs). Thereafter, another steep increase in the current occurs, and the current finally reaches a quasi-steady-state (though turbulent) value at $T = 40$ (0.3 μs). At the beginning, only slightly energized plasma electrons in the immediate environment hit and discharge the solar cell surface. Their energy is not sufficient to generate secondaries and the current scales with pure particle collection (Fig. 9b). At $T = 20$, the target is hit by electrons that have an origin in more remote locations of the system. They are accelerated by the electric field for a sufficiently long time to gain enough energy to generate secondaries upon impact. The transition region reflects dynamic processes in the sheath and on the dielectric surface (see III. B). With the impact of even more energetic electrons from the distant simulation regions, the higher secondary yield leads to a further current increase. The final turbulent state of the current describes the statistical nature of the impact processes and is not a consequence of turbulence in the ambient plasma, which displays a rather laminar behavior due to the strong electric fields. The quasisteady state is characterized by a balance between impacting and emitted electrons. An equilibrium is possible because most of the emitted thermal electrons are collected by the interconnector, as dictated by the potential structure shown in Fig. 6c.

In comparing the results of runs PMIEC and PMIEC1 in Table 1, we found that the anomalous current collected by the interconnector is not very sensitive to the angular velocity distribution of the emitted electrons. The formation of almost planar potential structures in front of the solar cell cover glass is also observed in these runs. They cause mainly normal incidence of the primary electrons, and no angular variation becomes evident. Only close to the interconnector, where the equipotential lines are more circular, does the angle of incidence lead to different emission properties (yield). Therefore, we observe a high current fluctuation level for a strong angular dependence ($\cos^{-1}\theta$ for run PMIEM) and a decreasing fluctuation level for a weaker angular dependence ($\cos^{-1/2}\theta$ for run PMIEC and 1 for run PMIEC1). The equilibrium "average" current level, however, is comparable for all three cases. A higher rate of emitted secondary electrons due to a more oblique incidence of the primary electrons, therefore, does not increase the average anomalous current level. The ambient and surface potential structures form in such a way that the balance between emitted and incoming electrons is conserved on a time-averaged basis.

D. Particle Distribution

Snapshots of the particle distribution in the system are shown in Figs. 10a–10d. For $\phi_0 = 100$ V at $T = 200$ (1.5 μs), the electrons are essentially uniformly distributed in the system. Only close to the solar cell surface do the particles give evidence for shielding and discharging processes. As mentioned before, the dielectric eventually becomes negative with a slightly negative potential. Therefore, an electron density depletion is observed near the dielectric which increases in its spatial extent toward the center of the solar cell (see Fig. 10a). The ions show a pronounced density cavity around the interconnector (see Fig. 10b), which results from the repelling action of the sheath on positive charges. The large initial electric field in the system is able to accelerate the heavy ions within a rather short time of 1.5 μs, and this indicates the need for realistic mass ratios. In the temporal evolution, the ions are accelerated toward the upper boundary creating enhanced densities at that location. As the electric field contracts and is gradually confined to the sheath, ions can re-enter the lower part of the system. This refilling process, however, will take a relatively long time since now the ions only move according to their thermal motion.

A larger applied potential of 250 V gives basically the same distribution for the electrons (see Fig. 10c), with a more pronounced triangular shaped density depletion across the cover glass surface (compare Figs. 10a and 10c). With the larger surface potential, more plasma electrons are required to discharge the increased polarization surface charges. This results in the overall decrease in the electron density in the system of Fig. 10c relative to that in Fig. 10a.

For secondary emission, the electrons are distributed as shown in Fig. 10d. The large electric field that persists in the system creates a density cavity in front of the target surface, where the electric field strength is weakest. The formation of this density cavity regulates the current balance between the incoming plasma electrons and the emitted electrons. The secondaries are visible close to the surface. With only thermal energies, they cannot penetrate deep into the plasma environment. Because of the potential structure near the solar cell surface (see Fig. 6c), part of the emitted electrons are accelerated toward the interconnector. Surface potentials of 150 to 220 V provide an emission rate between 2 and 3 secondary electrons for each impacting plasma electron. Incoming plasma electrons are therefore balanced by emitted secondary electrons, half of which are reflected back to the cover glass and part of which are subsequently collected by the interconnector. It is anticipated that more energetic secondary electrons will result in more escaping electrons and a reduced rate of reflected particles. In this case, equilibrium will be reached for a reduced surface potential and a lower secondary electron yield (close to 1).

IV. Summary and Discussion

Our calculations demonstrate that PIC simulations with the "real" ion mass can treat the solar array/plasma interaction

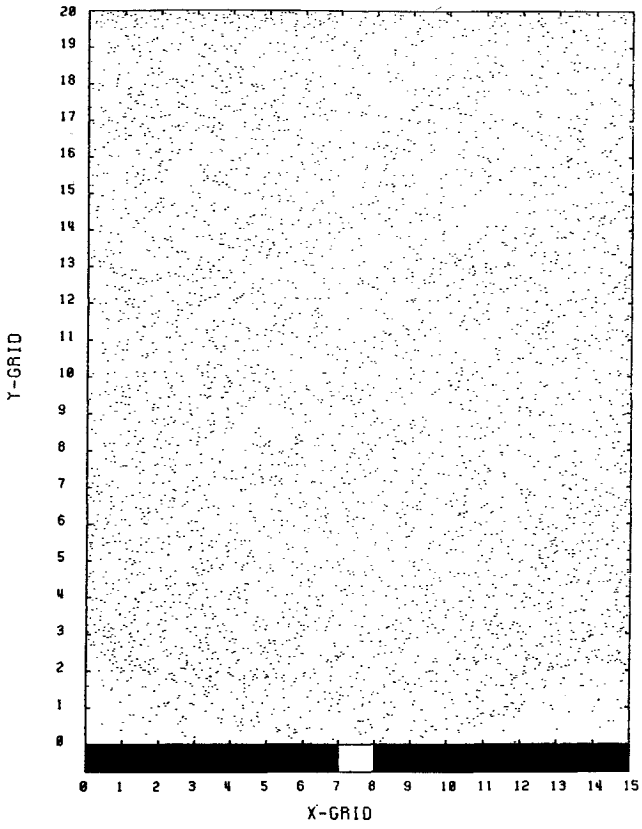

Fig. 10a Electron distribution for $\phi_0 = 100$ V at $T = 200$.

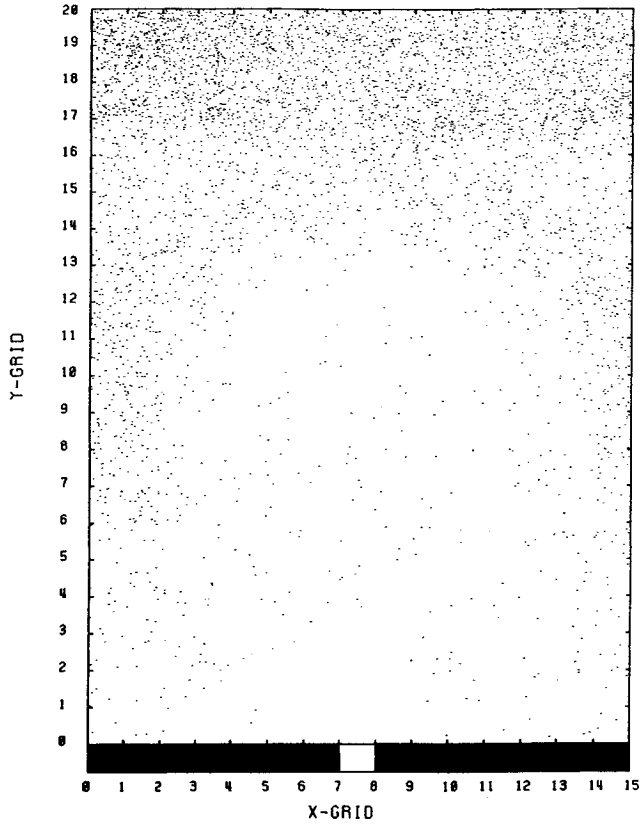

Fig. 10b Ion distribution for $\phi_0 = 100$ V at $T = 200$.

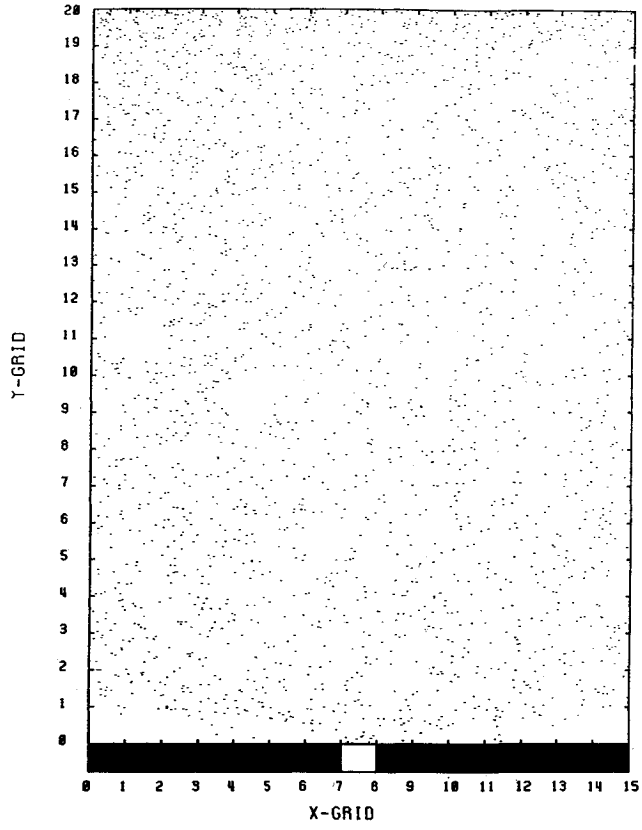

Fig. 10c Electron distribution for $\phi_0 = 250$ V at $T = 200$.

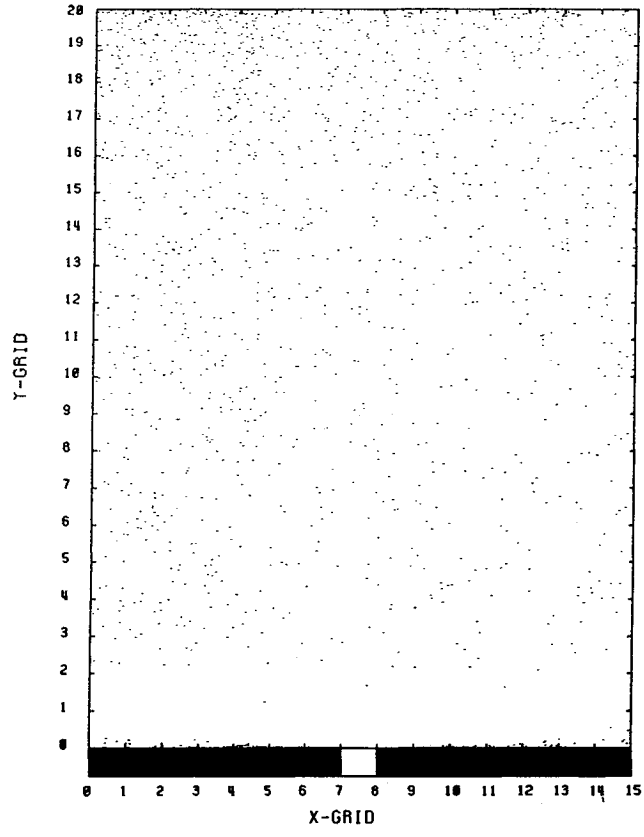

Fig. 10d Electron distribution for $\phi_0 = 250$ V with secondary electron emission at $T = 150$.

problem within a reasonable computational time. The simulations could be run for a sufficiently long time to achieve a steady-state, which is the time it takes for the collected current to reach a constant level. Our simulations indicate that the time to reach a steady-state scales directly with both the applied voltage and the system size, and inversely with the coverglass thickness. Because we used the real ion mass and a fine spatial grid near the cover glass and interconnector regions, we were able to obtain a detailed picture of the physical processes

(sheath formation, surface charges and potentials, collected current, etc.) as a function of time for the biased solar array problem. For example, we were able to show, for the nonemitting case, that there are three distinct regions on the cover glass that display different discharging features. Such a comprehensive picture has not been presented before.

Although realistic PIC simulations can be conducted, they do require substantial computer resources. For the simulations presented in this paper, we used the CRAY-XMP and CRAY-2 computers. The net CPU-time for a typical run of 200 plasma periods and the system size of Fig. 4 was 6 h. Therefore, computer constraints limit the number of possible runs one can consider. In this study, simulations were conducted for both 100- and 250-V solar cells, an extended simulation domain, two solar cell thicknesses, and solar cells with secondary electron emission.

Our simulations indicate that the sheath formation around interconnectors attached to high voltage solar arrays in an LEO plasma differs considerably from that predicted by Langmuir probe theory for the same voltage (see Table 2). The reason our simulation results differ from simple probe theory is because the complex material structure (plasma, conducting interconnector, dielectric cover glass) with different electrical properties influences the sheath formation. The combined action of interconnector shielding and dielectric discharging, both in competition with each other, results in perpendicular (to the solar cell) sheath dimensions that typically differ by one order-of-magnitude from simple probe theory. In the direction parallel to the solar cell, the difference is even larger. Without secondary electron emission from the cover glass, the perpendicular sheath radius and the current collected by the interconnector are directly related to the applied potential. However, with secondary emission, a planar potential structure forms in front of the interconnector and solar cells, and the interconnector current increases by a factor of 5 due to the collection of secondaries generated in the contact region of the solar cell.

It is useful to discuss our simulations with secondary electron emission, where we get planar potential structures, in the light of the "snapover" phenomenon. Snapover refers to the anomalously large increase in collected current that occurs when solar cells are biased above a critical positive voltage. This voltage has been termed the snapover voltage from the S shape of the current-voltage curve for the conductor. The increased current is due to the production of secondary electrons from the cover glass surface.[10] A possible explanation for this phenomenon was provided by Stevens[4] using a simple sheath model. Assuming that each interconnector in a solar array had its own hemispherical sheath, Stevens argued that as the applied voltage is increased, the individual sheaths expand radially and eventually overlap forming a planar potential structure that favors secondary electron production. The voltage at which the sheaths overlap corresponds to the snapover voltage, and it depends on the size of the solar cells. For 2×2 cm solar cells, Stevens calculated overlapping sheaths for about $+100$ V. However, in our simulations involving secondary electron emission, the interconnector voltage was instantaneously applied, and hence, a planar potential structure existed at the beginning of the simulations. This potential configuration acted to accelerate the plasma electrons toward the cover glass, which in turn led to the production of secondary electrons. These secondary electrons then acted to maintain the planar potential structure and a quasi-steady state was quickly achieved. How this scenario relates to the snapover phenomenon is uncertain. For example, it is not clear if we would get the same result if the rise-time of the applied voltage is long compared to the electron plasma period so that individual sheaths could start to form before the applied voltage increases beyond the snapover voltage.

The above discussion on the snapover phenomenon indicates the complexity of solar array/plasma interaction problems. This complexity is further illustrated when we attempt to compare our simulations with our laboratory experiments.[8] Specifically, the potential distributions obtained from our simulations seem to contradict the empirical model deduced from our laboratory experiments. The measurements indicated potential structures that are more similar to the theoretical results for no secondary electron emission. The difference between the results is not related to errors in either the model or the measurements but rather to differences in the input parameters. For the model, the potential was instantaneously applied to the solar cell, whereas in the experiment, the potential reached its peak value after a few tens of microseconds. This is a relatively long time with regard to the plasma response (several nanoseconds). The discharging of the solar cells is different for the two situations, and, hence, different potential structures are anticipated. Our present model results are applicable to relatively rapid potential rise times. Simulations are in progress that involve longer potential rise times, and laboratory tests are also in progress that involve rapid potential rise times. Eventually, theory-measurement comparisons will be possible for both cases. However, another possible reason for the difference between our model predictions and measurements could be related to the size of our simulation system. Larger systems might be needed for the cases with secondary electron emission, but this would greatly increase the computer requirements. It is clear that much work still remains before all the interaction processes are fully elucidated.

The simulations also have practical applications. They suggest that more experimental work is needed to study the dynamic current behavior at the beginning of the potential switch-on phase, where a large current surge can occur.[15] This requires a particularly high temporal resolution in the 0.1 μs range. Since the initial plasma response is very important in determining the overall plasma-dielectric interaction, an improved temporal resolution for the measurements will also provide valuable data on the small-scale plasma processes. Finally, a code developed and tested for a variety of plasma environments, emission properties, material, and geometries will serve as an important tool for providing design guidelines for solar arrays in the LEO plasma.

Acknowledgments

This research was supported by NASA grant NAG3-792 and AFOSR contract F49620-86-C-0109 to Utah State University and European Space Agency grant 6469/85/NL/1W to Physikalisch-Technische Studien GmbH. We thank K. P. Bogus for fruitful discussions.

References

[1]Stevens, N. J., "Interactions Between Spacecraft and the Charged Particle Environment," NASA CP-2071, 1978, pp. 268-294.

[2]McCoy, J. E., and Konradi, A., "Sheath Effects Observed on a 10 Meter High Voltage Panel in a Simulated Low Earth Orbit Plasma," NASA CP-2071, 1978, pp. 315-340.

[3]Stevens, N., "Space Environmental Interactions with Biased Spacecraft Surfaces, Space Systems and their Interactions with Earth's Space Environment," edited by H. B. Garrett and C. P. Pike, Vol. 71, *Space Systems and Their Interactions with Earth's Space Environment*, Progress in Astronautics and Aeronautics, AIAA, New York, 1980.

[4]Stevens, N., "Review of Biased Solar Array-Plasma Interaction Studies," NASA TM-82693, 1981.

[5]Gabriel, S. B., and Garner, C. E., "Experimental Measurements of the Plasma Sheath Around Pinhole Defects in a Simulated High-Voltage Solar Array," AIAA Paper 83-0311, 1983.

[6]Thiemann, H., and Bogus, K., "Anomalous Current Collection and Arcing of Solar-Cell Modules in a Simulated High-Density Low-Earth-Orbit Plasma," *ESA-Journal*, Vol. 10, 1986, pp. 43-57.

[7]Thiemann, H., and Dharma Rao, P. V., "Anomalies Observed in Plasma-Module-Interaction Experiments," *Proceedings of the 5th European Symposium: Photovaltaic Generators in Space*, European Space Agency, Noordwijk, the Netherlands, ESA SP-267, 1986.

[8]Thiemann, H., and Bogus, K., "High Voltage Solar Cell Modules in Simulated Low-Earth-Orbit Plasma," *Journal of Spacecraft and*

Rockets, Vol. 25, No. 4, July–Aug. 1988, pp. 278–285.

[9]Nonnast, J. H., Chaky, R. C., Armstrong, T. P., Enoch, J., and Wiseman, C. J., "Numerical Simulation of Plasma-Insulator Interactions in Space, Part I: The Self-Consistent Calculation," NASA CP-2182, 1980, pp. 932-945.

[10]Chaky, R. C., Nonnast , J. H., Armstrong, T. P., Enoch, J., and Wiseman, G. G., "Numerical Simulation of Plasma-Insulator Interactions in Space, Part II: Dielectric Effects," NASA CP2182, 1980, pp. 946-956.

[11]Brandon, S. T., Kessel, R. L., Enoch, T. P. and Armstrong, T. P., "Numerical Simulations of Positively Biased Probes and Dielectric Conductor Peaks in a Plasma," *Journal Applied Physics*, Vol. 56, 1984, pp. 3215–3222.

[12]Kessel, R. L., Murray, R. A., Hetzel, R., and Armstrong, T. P., "Numerical Simulation of Positive-Potential Conductors in the Presence of a Plasma and a Secondary-Emitting Dielectric," *Journal of Applied Physics*, Vol. 57, 1985, pp. 4991–4995.

[13]Kuminaka, H., and Kuriki, K., "Numerical Analysis of Interaction of a High-Voltage Solar Array with Ionospheric Plasma," *Journal of Spacecraft and Rockets*, Vol. 24, No. 6, Nov.–Dec., 1987, pp. 512–517.

[14]Levy, L., Sarrail, D., and Signeir, J. M., "Conductivity and Secondary Emission Properties of Dielectrics as Required by NASCAP," European Space Agency, Noordwijk, the Netherlands, EPA SP-232, 1985.

[15]Thiemann, H., Schunk, R. W., and Gerlach, L., "Solar Arrays in the LEO-Plasma Environment: A Model for Leakage Current Phenomena Deduced from Experimental and Theoretical Studies," *Proceedings of European Space Power Conference,* European Space Agency, Noordwijk, the Netherlands, 1989.

Color reproduction courtesy of Utah State University